Phiri, Josphat; Johansson, Leena Sisko; Gane, Patrick; Maloney, Thad C.

Co-exfoliation and fabrication of graphene based microfibrillated cellulose composites-mechanical and thermal stability and functional conductive properties

Published in:
Nanoscale

DOI:
10.1039/c8nr02052c

Published: 28/05/2018

Document Version
Peer-reviewed accepted author manuscript, also known as Final accepted manuscript or Post-print

Please cite the original version:
Phiri, J., Johansson, L. S., Gane, P., & Maloney, T. C. (2018). Co-exfoliation and fabrication of graphene based microfibrillated cellulose composites-mechanical and thermal stability and functional conductive properties. *Nanoscale*, *10*(20), 9569-9582. https://doi.org/10.1039/c8nr02052c

Nanoscale

Accepted Manuscript

This article can be cited before page numbers have been issued, to do this please use: J. Phiri, L. Johansson, P. Gane and T. Maloney, *Nanoscale*, 2018, DOI: 10.1039/C8NR02052C.

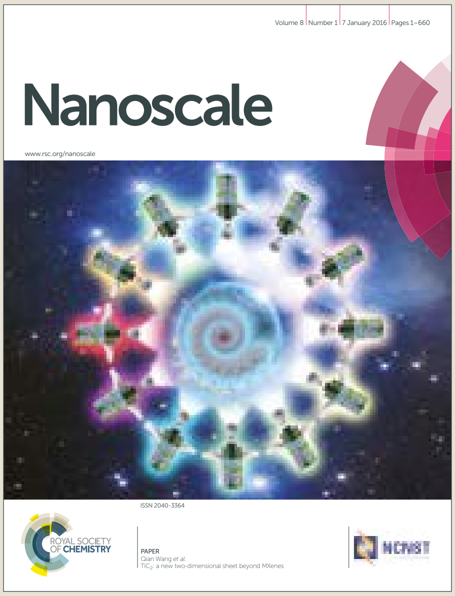
Volume 8 | Number 1 | 7 January 2016 | Pages 1–660

Nanoscale

www.rsc.org/nanoscale

ISSN 2040-3364

ROYAL SOCIETY OF CHEMISTRY

PAPER
Qian Wang et al.
TiC_2: a new two-dimensional sheet beyond MXenes

ROYAL SOCIETY OF CHEMISTRY

rsc.li/nanoscale

View Article Online
DOI: 10.1039/C8NR02052C

Co-exfoliation and Fabrication of Graphene Based Microfibrillated Cellulose Composites - Mechanical, Thermal Stability and Functional Conductive Properties

Josphat Phiri[1*]; *Leena-Sisko Johansson*[1]; *Patrick Gane*[1, 2]; *Thad C. Maloney*[1*]

[1]School of Chemical Engineering, Department of Bioproducts and Biosystems, Aalto University, P.O.
Box 16300, 00076 Aalto, Finland
[2]Omya International AG, CH-4665 Oftringen, Switzerland

*Corresponding Authors: josphat.phiri@aalto.fi (J. Phiri); patrick.gane@omya.com (P. Gane); thaddeus.maloney@aalto.fi (T. Maloney)

View Article Online
DOI: 10.1039/C8NR02052C

Abstract

The excellent functional properties of graphene and micro nanofibrillated cellulose (MNFC) offer plenty of possibilities for wide ranging applications in combination as composite material. In this study, flexible graphene/microfibrillated cellulose (MFC) composite films were prepared by a simple method of co-exfoliation of graphite in MFC suspension by high-shear exfoliation. We show that pristine graphene, without any chemical treatment, was homogeneously dispersed in the MFC matrix, and the produced composites showed enhanced thermal, electrical and mechanical properties compared to a non-co-exfoliated control. The film properties were studied by XPS, XRD, Raman, SEM, FTIR, TGA, nitrogen sorption, UV-vis spectroscopy, optical and formation analysis tests. At 0.5 wt% loading, the specific surface area of graphene/MFC composites increased from 218 to 273 m^2 g^{-1} while the tensile strength and Young's modulus for the graphene/MFC composites increased by 33 % and 28 % respectively. Thermal stability was enhanced by 22 % at 9 wt% loading and the composites showed a high electrical conductivity of 2.4 S m^{-1}. This simple method for the fabrication of graphene/MFC composites with enhanced controlled functional properties can prove to be industrially beneficial, and is expected to open up a new route for novel potential applications of materials based largely on renewable resources.

Keywords:

Nanocomposites, microfibrillated cellulose, nanofibrillated cellulose, graphene, graphene oxide, reduced graphene oxide

View Article Online
DOI: 10.1039/C8NR02052C

1. Introduction

Graphene is a one-atomic thick layer of carbon atoms arranged in a honeycomb hexagonal lattice. It has attracted tremendous research and commercial interest due to its exceptional properties, such as high surface area, excellent thermal and electrical conductivity, high mechanical strength and barrier properties etc. [1-4]. As a building block, graphene has been widely used to prepare various functional materials with precisely tailored properties [5, 6], including humidity sensors, composites, energy storage devices, catalysts etc. [3, 7-9]. Theoretically, monolayered functionalized graphene is by far the best functional filler component for all potential reinforcements due these properties [10] and, as such, it has been used in various graphene/polymer composites, not only to enhance the existing polymer properties but to introduce new otherwise unachievable properties in polymer-based materials science [8, 11-14]. One advantage of using graphene in nanocomposite fabrication is that at even very low loading, a significant increase in the multifunctional properties is observed when compared to conventional fillers. The resulting mechanical properties are due to its extremely high aspect ratio and increasing interfacial molecular bond between graphene sheets and the host matrix, both contributing to the strengthening and bending resilience effect [15].

Compared to carbon nanotubes, graphene has emerged as a viable option for polymer reinforcement. Since their discovery, carbon nanotubes application in polymer reinforcements has been limited and challenging. This is because carbon nanotubes are still expensive to fabricate, have poor aqueous dispersibility and poor interfacial molecular bonding with the polymer matrix [16] and, thus, in many cases do not lead to the sought-after enhancement of properties. However, despite being a more recent material discovery than carbon nanotubes, graphene has already shown a lot of promise as a feasible and economical option for fabrication of highly efficient polymer based composites.

Natural polymer micro and nanostructures, such as cellulose-based materials, have gained increasing interest for wide scale application due to their renewability and biodegradability, low cost

View Article Online
DOI: 10.1039/C8NR02052C

and density, interesting mechanical properties, non-toxicity etc. [17-19]. However, most of the functional properties required for the next generation applications in engineering, medical, printed and electronic industries, for example, cannot be provided by purely cellulosic-based materials [17]. In order to meet the growing demand for sustainable materials, fillers having a nano-dimension with defined functional properties can be incorporated into the polymeric cellulose fibrillar matrix that enhance the existing properties of the cellulose-based material [19]. The produced composites can be tailored for specific application by controlling the type and amount of filler used, production method, surface chemistry of the filler and the cellulose matrix.

Cellulose materials such as micro nanofibrillated cellulose (MNFC) have shown to be ideal for composite fabrication due to their specific surface chemistry that makes them compatible with various nanofillers. The surface of MNFC is rich with –OH and CH functional groups that promote grafting with various nanofillers, and give MNFC its amphiphilic properties. It is important to note that compatibility of the filler and polymer matrix is vital for the overall performance of the produced composites. Excellent compatibility between the polymer matrix and nanonofiller leads to a high interfacial molecular interaction and thus increases the stress transfer between the filler and the matrix. Moreover, this also promotes the homogeneous dispersion of nanofiller in the polymer matrix.

Graphene and its derivatives graphene oxide (GO) and reduced graphene oxide (RGO) have been incorporated into aqueous cellulose dispersion to produce matrix composites with enhanced properties. Oxidised graphene is the popular choice for this application due to the presence of oxygen functional groups on the surface and edges that promote compatibility with the polar polymeric matrix. A major portion of prior reported work involves utilisation of GO or RGO as nanofillers in such cellulose matrices. GO is prepared by oxidation of graphite, in practice based on a variety of modified protocols [20, 21]. GO is then reduced to form RGO, and the dispersions are formed by sonication in water/solvent solutions.

View Article Online
DOI: 10.1039/C8NR02052C

Even though GO and RGO make very compatible fillers for polymer composite fabrication, they do not exhibit many of the exceptional properties attributed to pristine graphene. Therefore, there is still a need to find better methods for fabrication of graphene/polymer composites that can make use of the excellent properties of pristine graphene in composite materials, whilst generating sufficient compatibility between the graphene and the host cellulosic material to form an integral composite.

Wider scale application of graphene has been hindered due to lack of viable and efficient fabrication methods. The desirable methods for graphene production especially for composite application are those that utilise graphite as a raw material. Graphite is a natural material that is relatively low-cost and abundant [22]. Pristine graphene dispersions, i.e. adopting graphene produced without oxidation processes, are normally produced by liquid phase exfoliation methods, such as sonication or by shear exfoliation of graphite in solvent or surfactant media [23]. However, low yield, high cost and toxicity of solvents makes this method not viable for wider applications. Besides, most of the surfactants used are not suitable for composite fabrication and the solvents are not only expensive but also ecologically unfriendly [24]. Therefore, there is a dire need for utilisation of green materials for fabrication of highly functional composites using feasible methods.

In this study, graphite is directly exfoliated to graphene in aqueous MFC suspensions by the application of high shear. It has been shown in our earlier study, and other studies that shear exfoliation can be used to form few-layer graphene sheets in surfactant and polymer solutions [25-27]. The suspensions are then used to produce functional graphene/MFC composites. As a reference material, RGO powder is also exfoliated in MFC suspension and compared to graphene based MFC films. Theoretically, the surface chemistry of RGO allows for the formation of more interesting MFC composites with enhanced properties. Therefore, as a reference material, it will be used to compare how well graphene/MFC composites perform in comparison with RGO reinforced MFC composites, which is a well-accepted filler material due to the presence of functional groups. Direct exfoliation of

View Article Online
DOI: 10.1039/C8NR02052C

graphene in MFC suspensions offers many advantages, including composites based completely on largely renewable materials that are low cost, easily available, biodegradable and with excellent various functional properties. This simple approach of high performance fabrication of composites offers potential for a wide range of application.

2. Materials and methods

2.1. Materials

Natural graphite was kindly provided by Asbury Carbons, Product Number: GNP nano307, hydrochloric acid (36 wt%), sulphuric acid (95-97 %), ascorbic acid (≥99 %), sodium hydroxide (1M) were purchased from Sigma Aldrich. Potassium permanganate (99 %) was supplied by J.T. Baker.

Microfibrillated cellulose was provided by Suzano Pulp and Paper at 5 wt% solids. The MFC was a relatively course grade produced by mechanical defibrillation of hardwood Kraft pulp. The length weighted average fibre length was 0.52 mm measured using FiberLab from Metso Automation. All the chemicals were used without any modification. Deionised water (DI) was used throughout the experiments.

2.2. MFC characterisation

The shear viscosity of diluted MFC suspension was measured by a Brookfield viscometer model DV2TRV Extra, using a V-72 vane spindle at 1.5 % solid consistency. Transmittance was measured using Shimadzu UV-Vis spectrophotometer 2550 at wavelengths 200 – 900 nm at 0.1 % MFC consistency. The experiments were conducted according to the procedures given by Kangas *et al*. [28]. Zeta-potential was measured using a Zetasizer Nano ZS instrument (Malvern Instruments Ltd.) at 0.1 % MFC consistency. To measure the water retention value (WRV), MFC was mixed with pulp and adjusted to 10 % consistency. The WRV measurements were conducted following the procedure reported by Maloney [29]. The measured parameters are summarised in Table 1.

View Article Online
DOI: 10.1039/C8NR02052C

Table 1 Properties of MFC

Shear viscosity /mPa.s (10 min^{-1} (rpm), 1.5 % consistency)	13 283
Transmittance /% (800 nm, 0.1 % consistency)	23.88 ± 0.58
Water retention value /cm^3 g^{-1}	4.49 ± 0.06
Zeta potential /mV (0.1 % consistency)	-31.6 ± 0.84

2.3. Preparation of RGO powder

RGO was prepared using a modified Hummers method [20]. Concentrated sulphuric acid (200 cm^3) was added to a 1 000 cm^3 flask immersed in an ice bath. Then, 10 g of natural graphite flakes were added with continuous stirring. After 5 min of mixing, 30 g of potassium permanganate was slowly added to the mixture to keep the temperature around 15 °C. The ice bath was then removed and stirring continued for 30 min. The mixture was then heated to around 40 °C in a water bath and kept there for 2 h. Next, the mixture was cooled down to room temperature followed by the addition of 200 cm^3 DI water that led to an exothermic reaction and a rise of temperature to about 80 °C. The mixture was again transferred to a water bath at 95 °C and kept for 2 h. After cooling down to room temperature, excess sulphuric acid was filtered off and the pH of the mixture was adjusted to 7-8 using sodium hydroxide. Then, 40 g ascorbic acid was dissolved in 200 cm^3 DI water and subsequently added to the mixture. The mixture was transferred to a water bath and heated at 95-98 °C for 2 h to reduce GO to RGO. The mixture, still immersed in the water bath was left overnight to cool down. The product was filtered and washed with 10 % HCl, followed by water until reaching neutral pH. RGO powder was obtained after freeze-drying.

2.4. Preparation of graphene/MFC and RGO/MFC suspensions

Exfoliation of graphene in MFC suspension was achieved using an IKA Magic Lab (1 dm^3 module micro-plant equipped with a single-walled open 1 dm^3 vessel) [25]. The MFC was first diluted to a consistency of 0.8 wt%. Subsequently, natural graphite and RGO powder were added, respectively, to

View Article Online
DOI: 10.1039/C8NR02052C

the suspension in various proportions to yield a solid filler content of 0.5, 1, 3, 5, 7 and 9 wt% with respect to that of solid MFC. The resulting mixtures were then subjected to high shear exfoliation for 60 min. The IKA Magic Lab was continuously cooled with running cold water to prevent overheating and the suspension temperature was maintained to around 25-30 ^{o}C. The prepared suspensions were then used to fabricate sheets.

2.5. Preparation of composite sheets

The composite sheets were prepared using a modified laboratory hand-sheet former with a pressurised top chamber [30]. A nylon membrane with 1 µm mesh openings was placed on top of the conventional steel wire to prevent the loss of material. The suspensions were controllably measured onto the drainage unit to reach a final basis weight of ~100 g m^{-2}. To ensure complete drainage of water from the sheets, the dewatering time was set to be 12 min. To prevent shrinkage during drying, the sheets were removed from the hand sheet former and put between two steel mesh wires. Two blotting papers were then placed on the outside of the sandwich structure. The sheets were subsequently dried in a hot press at 120 ^{o}C for 10 min applying a pressure of about 50 kPa.

2.6. Component and composite characterisation methods

2.6.1. UV-Vis spectroscopy

UV-Vis measurements were carried out using a Shimadzu UV-Vis spectrophotometer 2550 at wavelengths 200 – 800 nm. The dispersions were controllably diluted before the measurements.

2.6.2. Scanning electron microscopy (SEM)

The structure and morphology of the composite sheets was recorded using a Zeiss Sigma VP scanning electron microscope at 2 kV acceleration voltage. The films were first sputtered with a gold-palladium film before SEM measurements.

View Article Online
DOI: 10.1039/C8NR02052C

2.6.3. Transmission electron microscopy (TEM)

TEM analysis was conducted in a Tecnai 12 from FEI (Hillsboro, Oregon, USA) at 120 kV. The samples for TEM were prepared by drop casting of diluted suspensions on carbon coated copper grids and dried at room temperature.

2.6.4. Grammage formation measurements

The local grammage variation of the composite sheets was measured by a SCAN-test method based on beta ray absorption using a Beta Formation Tester (Ambertec, Finland). For each sample, 400 points with a step of 1 mm in both x and y-directions on the sheet covering an area of 19 × 19 mm^2 were measured. A lower formation number indicates greater uniformity. The specific formation, $F_{1g} (= F_\sigma/\sqrt{w})$ in $\sqrt{\mathrm{g}}\,\mathrm{m}^{-1}$, is the formation number, F_σ in $\mathrm{g\,m}^{-2}$, normalised with respect to the square root of sheet grammage, $\sqrt{w}$ in $\sqrt{\mathrm{g\,m}^{-2}}$.

2.6.5. Fourier transform mid-infrared photoacoustic spectroscopy (FTIR–PAS)

The chemical structure of the composite sheets was observed using a BIO-RAD FTS 6000 (Hercules, California, USA) spectrometer. A helium gas purging flow was introduced into the sample chamber for 5 min before measurement to reduce the noise. All spectra were scanned within the range 400 – 4 000 cm^{-1}, with 400 scans and a resolution of 32 cm^{-1}.

2.6.6. Raman analysis

Raman spectra were measured using a WITec alpha300 R Raman microscope (alpha 300, WITec, Ulm, Germany) equipped with a piezoelectric scanner using a 532 nm linear polarised excitation laser. The analysis was made on the raw materials and on the surface of the composite films with a 9 wt% filler loading.

View Article Online
DOI: 10.1039/C8NR02052C

2.6.7. X-ray photoelectron spectroscopy (XPS)

The surface chemical composition of graphite, GO and RGO sheets as well as the 9 wt% composites were analysed with XPS, using an AXIS Ultra spectrometer with monochromatic Al Kα irradiation at 100 W, under neutralisation. Pure cellulose filter paper (Whatman) was measured with every sample batch as an in-situ reference for XPS experiments; in this study, it was also used as a reference for cellulose. Before the measurements, the samples were evacuated overnight. Survey scans as well as C 1s and O 1s high-resolution regions were acquired from 2-3 locations; the analysis area was less than 1 mm^2 while the analysis depth is less than 10 nm. CasaXPS software was utilised for data analysis in which the carbon and oxygen content was each determined from survey scans, while carbon high-resolution data ware utilised in further chemical analysis; for the fitting parameters, see reference [31].

2.6.8. X- ray diffraction (XRD)

XRD data were collected using a Rigaku Smart Lab X-ray diffractometer operating at 50 kV and 200 mA. The diffractograms were obtained using a scanning rate of 1.5 ^{o} min^{-1} in the 1D-mode of a 2-dimensional HyPix-3000 detector. The wavelength of the X-ray beam was 0.154 nm.

2.6.9. Thermogravimetric (TGA) and differential analysis (DTG)

The thermal stability of the composites was characterised by thermogravimetric analysis (TA Instruments Q500). All measurements were conducted under a nitrogen flow rate of 60 cm^3 min^{-1} over a temperature range of 25–800 °C with a heating rate of 10 °C min^{-1}.

2.6.10. Optical properties

The optical properties of the films were measured using an L&W Elrepho SE 070R Spectrophotometer at 395 nm wavelength.

View Article Online
DOI: 10.1039/C8NR02052C

2.6.11. Mechanical properties

The mechanical properties of the composite sheets were measured with an MTS-400/M testing system equipped with a 200 N cell load. The gap length was set to 5 cm and elongation rate to 12 mm min^{-1}. Eight strips with dimensions 70 × 15 mm^2 were cut from the sheet and used for measurements for each point. Prior to the measurements, the samples were stored in a controlled atmosphere (23 ^oC; 50 % RH) for 48 h.

2.6.12. Nitrogen adsorption measurements

Surface area and pore volume of the composites were determined using a Micromeritics Tristar II. The samples for surface area analysis were prepared by solvent exchange and critical point drying (CPD). Briefly, after removing excess water, the composites were solvent exchanged in acetone for 72 h. Acetone was periodically changed during this process. Immediately after this process, the samples were transferred into a Leica EM CPD300 for CPD in liquid CO_2. After drying, the samples were immediately transferred to the Micromeritics Tristar II device for nitrogen sorption measurements.

2.6.13. Electrical conductivity

Electrical conductivity of the composite sheets was measured with a four-point probe method (Jandel RM3000: Jandel Engineering Ltd.). The measured resistance was converted to sheet resistance, R_s Ω $sq.^{-1}$, and the specific resistance, ρ, was then calculated from $\rho = R_s \times t$, where t is the film thickness in cm, and subsequently the corresponding electrical conductivity, $\sigma = 1/\rho$ (S cm^{-1}) was calculated.

3. Results and discussion

The UV-vis spectra of the MFC, MFC/graphene and MFC/RGO suspensions are shown in Figure 1A. A featureless spectrum is seen for the neat MFC samples. However, with the addition of

View Article Online
DOI: 10.1039/C8NR02052C

graphene and RGO, the typical characteristic peaks at around 270 nm are observed in the suspensions confirming the presence of the 2-dimesional material and successful integration of graphene and RGO in the MFC suspension matrix. This maximum peak at ~270 nm is attributed to the $\pi - \pi^*$ transition of aromatic C – C bonds in graphene. The peak also at 267 nm for RGO/MFC suspensions confirms successful reduction of graphene oxide, and is similar to that seen in another study [32]. These results confirm that graphene was successfully exfoliated from graphite and integrated in the polymeric MFC matrix suspension.

The Raman spectra of MFC, RGO and graphite, together with their composites at 9 wt% loading, are shown in Figure 1B. For graphite and graphene/MFC composites, the spectra showed a very pronounced G-band and much weaker D-band. However, the G-band for RGO and RGO/MFC composites broadened and shifted to 1 570 cm^{-1} and the D-band become more prominent. The detailed Raman parameters are shown in Table 2. The G-band is related to the relative vibration of sp^2 bonded carbon atoms, and indicates the presence of graphene, while the D-band is due to the ring breathing modes and is activated only in the presence of defects [33, 34]. The 2D band is the second order of the D-band, and is always present even in defect-free graphene [34]. The intensity ratio of the D and G bands (I_D/I_G) is used to estimate the carbon ratio sp^2/sp^3, which relates to the quantity of defects [35]. The ratio for pristine graphite is comparable to that of graphene/MFC composites after co-shear exfoliation of the two materials. Normally, when the suspensions are subjected to high shear exfoliation, there is a reduction of size in the graphite particles that leads to an increased amount of edge disorder present in the samples, which is detected by Raman [36]. When comparing the two spectra of pristine graphite and graphene/MFC samples, there are only subtle differences observed (Table 2). The D- and G-bands shifted upwards in wavenumber by about 5 cm^{-1} and 2 cm^{-1}, respectively, while the 2D-band shifted downwards by 2 cm^{-1} and the intensity almost doubled. It has been shown that, as the number of graphene layers are reduced the 2D maximum tends to shift to lower values and the intensity increases

View Article Online
DOI: 10.1039/C8NR02052C

[25, 37-39]. These indicators show that graphene was exfoliated in MFC suspensions and the subtitle changes observed confirm that the graphene structure is well preserved and incorporated into the MFC suspension matrix. Our earlier study of shear exfoliation of graphite in surfactant and polymer solutions showed a very significant increase of defects induced by shear exfoliation in graphene [25]. The lower defects in this study shows that MFC prevents detrimental structure damage of graphite during exfoliation.

The intensity ratio (I_D/I_G) increases with the quantity of defects present in the graphitic material. For RGO, significant increase is observed as compared to that of pristine graphite, indicating that oxidation induces defects in the material. Oxidation of graphite leads to an increase in the amount of sp^3 carbon bonds, structural and edge defects, and introduces functional groups into the graphitic carbon chain, which all contribute to the intensity of the D-band. However, the D-band intensity reduced after shear exfoliation of RGO in MFC suspensions, indicating a higher degree of graphitisation [37] and a reduction of structural disorder. It is still unclear why this reduction was observed, but, possibly during shear exfoliation, the continuous strong interfacial interaction/friction of MFC and RGO sheets promotes a restoration of the graphene structure. It is probably the case that there is a restoration of sp^3 to sp^2 carbon bonds during the high shear exfoliation of RGO in MFC suspensions. A more detailed study is required to comprehend this phenomenon fully.

Table 2 Raman parameters of the graphite and RGO powders together with their respective composites

Sample	D-band		G-band		2D-band		I_D/I_G
	Position /cm^{-1}	Intensity /a.u	Position /cm^{-1}	Intensity /a.u.	Position /cm^{-1}	Intensity /a.u.	
Graphite	1 340.67	42.13	1 568.40	140.22	2 684.72	43.64	0.30
RGO	1 335.74	206.46	1 570.79	153.70	2 680.58	19.33	1.34
MFC/RGO	1 335.74	112.88	1 566.01	145.44	2 670.22	41.28	0.78

View Article Online
DOI: 10.1039/C8NR02052C

Graphene/MFC	1 345.57	56.88	1 570.79	246.18	2 682.65	75.46	0.23

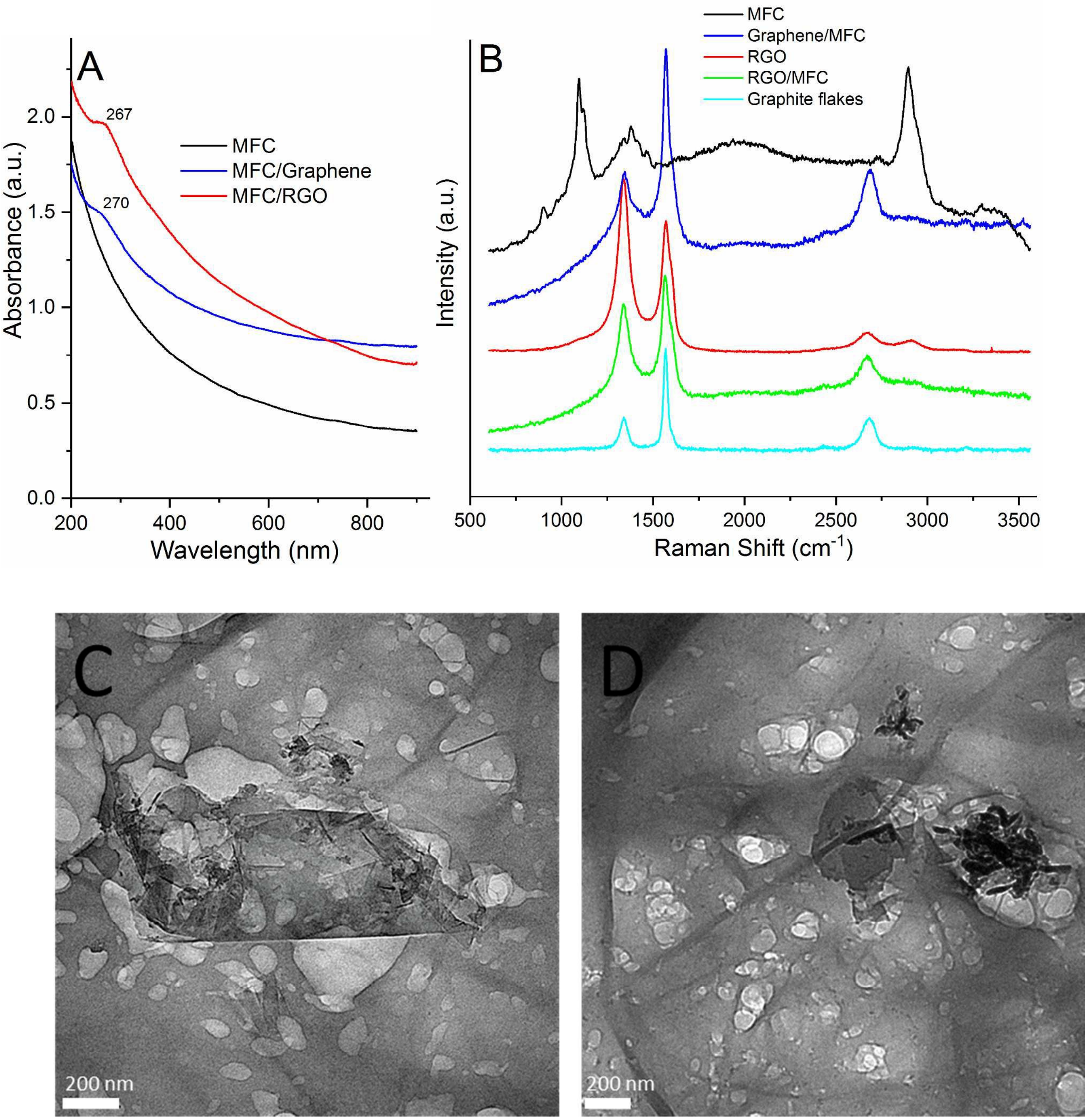

Figure 1 (A) UV-vis spectra of MFC, MFC/graphene and MFC/RGO suspensions; (B) Raman spectra of MFC; TEM images of (C) folded graphene sheet in MFC, and (D) RGO sheet embedded in the MFC matrix

View Article Online
DOI: 10.1039/C8NR02052C

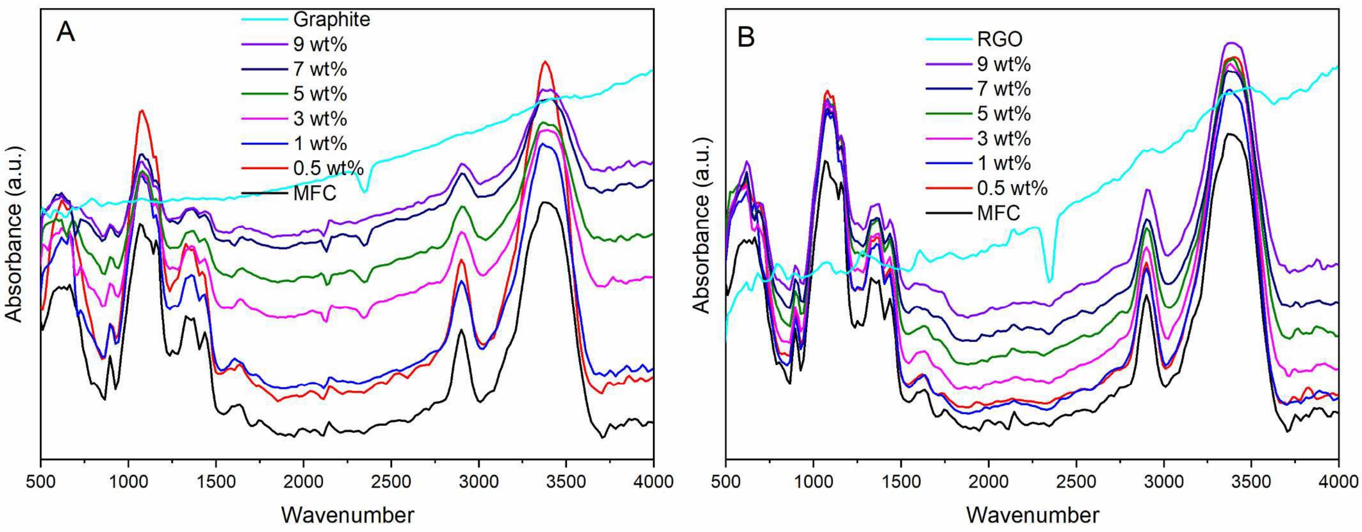

Figure 2 FTIR analysis of (A) graphene/MFC and (B) RGO/MFC composites with filler loading of 0.5, 1, 3, 5, 7 and 9 wt% in comparison with neat MFC, graphite and RGO samples

To study the exfoliation of graphene and the level of sheet blending/dispersion in the MFC composites, TEM image analysis was used. It is important to note that by blending, the authors refer to enabling sufficient contact to be developed between the filler and the cellulose matrix, and not a measure of homogeneity of the mix, which in the cases of strong hydrophobicity could never be the case. The TEM images of both MFC/graphene and MFC/RGO composites are shown in Figure 3 and Figure S2. These images confirm the presence of few-layer graphene sheets embedded in the MFC matrix as well the presence of large unexfoliated graphite particles. The graphene sheets are sparsely dispersed in the matrix with lateral size distribution ranging from several nanometres to micrometres.

The FTIR analysis was employed to study the interaction between graphene and MFC. The FTIR spectra of the raw materials and produced composites are shown in

View Article Online
DOI: 10.1039/C8NR02052C

Figure 2. Compared to graphite, RGO showed characteristic infrared absorption peaks, because of the residual oxygen functional groups still present on the surface. The peak at around 1 725 cm^{-1} is due to the C=O moieties present in the structure, showing the presence of carboxyl/carbonyl functional groups. Other characteristic absorption peaks at ~1 610 cm^{-1} represent the skeletal in-plane vibration of C C groups, while at 1 190 cm^{-1} the epoxy groups C–O [40]. In both cases, with the incorporation of graphene and RGO, shifting and disappearance of some peaks from the MFC spectrum are observed confirming successful blending of the filler and the polymer matrix. The analysis of the hydroxyl (OH) of the composites can also clarify the interaction of the graphene and MFC matrix. At around 3 400 cm^{-1}, it has been shown that cellulose based materials contain intramolecular and intermolecular hydrogen bonds [41, 42]. It is clearly seen in

DOI: 10.1039/C8NR02052C

Figure 2 that, with the incorporation of the filler into the MFC matrix, a broader and higher intensity peak is formed which has been attributed to the formation of intermolecular hydrogen bonds between the filler and polymer matrix [43, 44]. Due to the presence of the functional groups on the RGO surface, which promote a hydrogen bond with the MFC matrix, the prominent increase in intensity is observed for the RGO/MFC composites. Similar results have been observed previously between graphene and cellulose based composites [44, 45].

Despite the presence of the functional groups in RGO (Table S2), the two spectra for the two composites, i.e. graphene/MFC and RGO/MFC are closely comparable, indicating that successful blending of graphene in the MFC matrix *via* high shear exfoliation was achieved.

XPS was used to study the surface chemistry of graphene/MFC and RGO/MFC composites. Figure 4 shows full XPS scan spectra together with high resolution C1s. Oxidation of graphene is clearly shown in surface compositions, both in wide spectra, where the oxygen surface content is increased from 5 at% to 20 at%, and in high resolution C 1s regional spectra, where the sharp asymmetric signal, centred around 284.3 eV, is transformed into cluster of components originating from carbon atoms with 0, 1, 2 or 3 bonds to oxygen neighbours. In the case of composite films, the high-resolution C 1s spectra in Figure 4B for both graphene/MFC and RGO/MFC are very similar.

View Article Online
DOI: 10.1039/C8NR02052C

This might indicate that both RGO and graphite exfoliated and blended/dispersed nicely into the MFC matrix despite that they both nominally have a very different surface chemistry (Table S2).

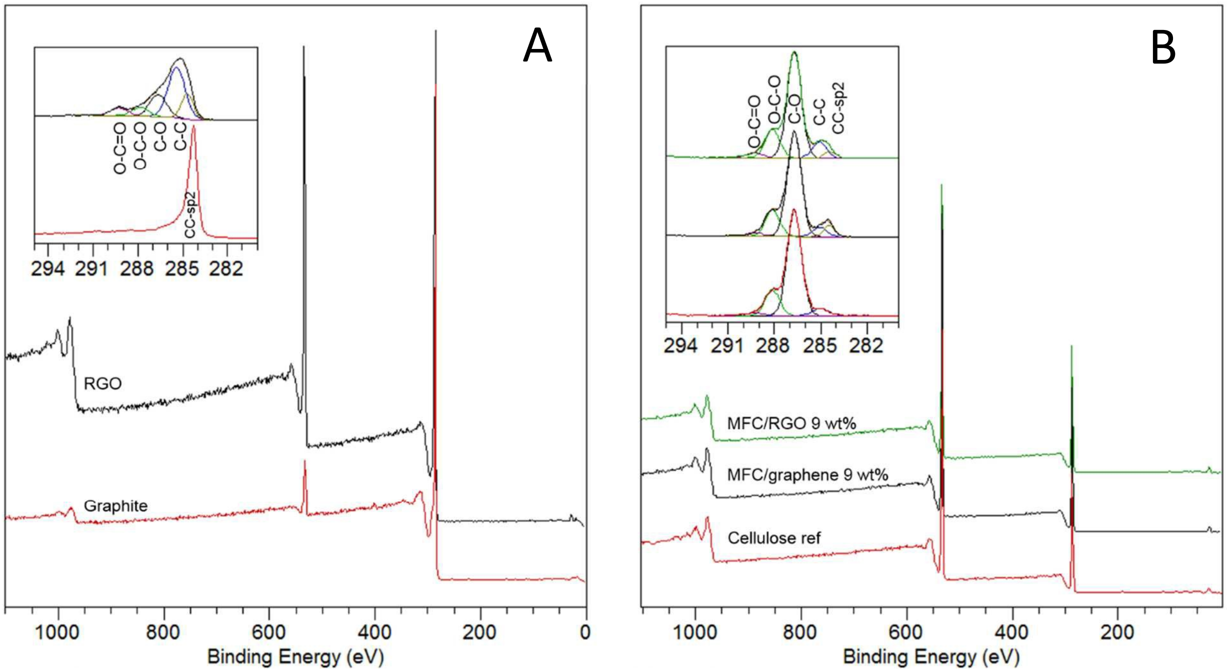

Figure 4 XPS analysis of wide scan and C1s HiRes (inserts) for (A) RGO and graphite and (B) graphene/MFC and RGO/MFC composites at 9 wt% loading.

XRD was used to study the phase structure and dispersion state of graphene in the MFC matrix. Figure 5 shows the XRD patterns of graphite, RGO and MFC together with their respective composites at different filler loadings. The neat MFC showed a typical characteristic cellulose I allomorph structure with a wide peak around $2\theta = 15.8^{o}$, 22.7^{o}, and 34.7^{o} [46]. It is observed that all the composites at all the various loadings preserve this structure. Graphite shows a peak at $2\theta = 26.4^{o}$ corresponding to a layer-to-layer *d*-spacing of 0.337 nm. However, the XRD pattern of RGO shows a broad peak (002) at $2\theta = 20$ to 30^{o} with a *d*-spacing of 0.358 nm. The higher *d*-spacing of RGO is due to the presence of oxygen functional groups, as shown by the FTIR and XPS analyses, and the peak broadening is caused by the poor ordering of RGO sheets along their stacking direction [47]. For graphene/MFC composites (Figure 5A), the graphite peak (002) completely vanished at lower concentrations and becomes only

View Article Online
DOI: 10.1039/C8NR02052C

slightly visible at 9 wt% loading. This indicates that graphite sheets uniformly exfoliated in the MFC matrix during the high shear exfoliation process. In addition, the peak for the functionalised RGO in MFC composites also disappears, which is an additional indication of exfoliation and uniform dispersion of RGO in the MFC matrix.

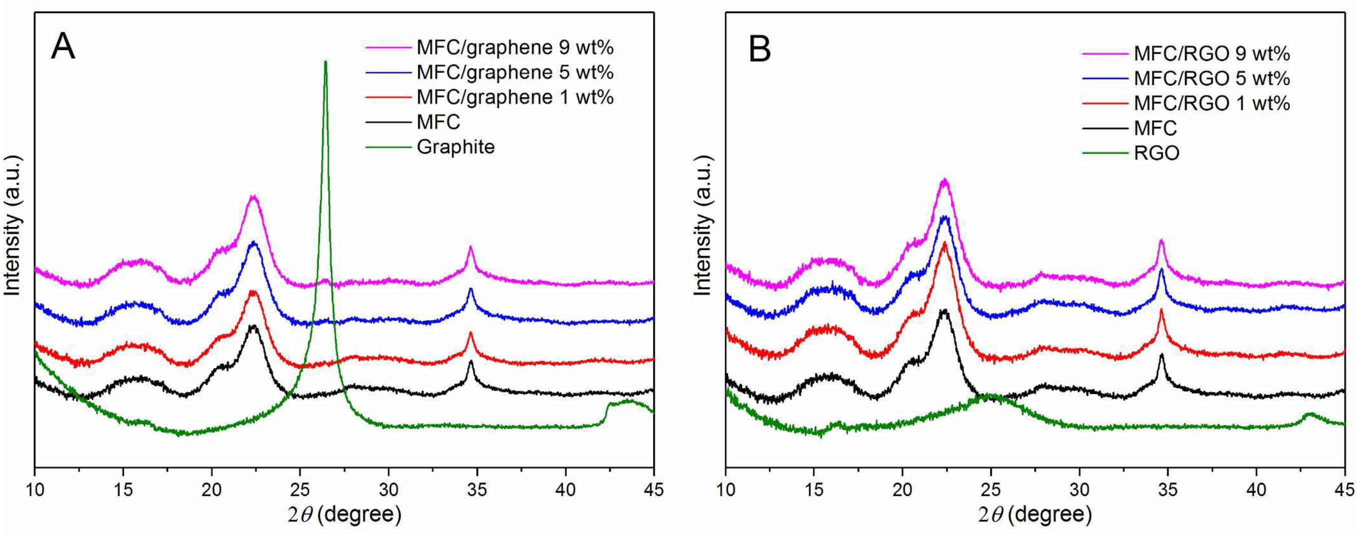

Figure 5 XRD patterns (A) graphene/ MFC and (B) RGO/MFC composites

The incorporation of RGO and graphene into the MFC matrix affects the crystallinity of MFC. It can be clearly seen from Table 3 that, with the addition of both graphene and RGO, the crystallinity of MFC composites changed. At lower filler loading, the graphene and RGO sheets aligned in parallel and facilitated an ordered alignment of MFC molecules leading to an increased crystallinity. However, at higher filler loading of 9 wt%, a decrease in crystallinity is observed. The higher filler content restricted the movement of cellulose molecules and led to the disordered orientation and organization of cellulose fibrils, thus displaying a decreased crystallinity. These findings are in agreement with other studies that also showed that crystallinity increases at lower loading and decreases at higher filler loadings [44, 48]. In particular, RGO/MFC reinforced composites showed a much greater decrease in

View Article Online
DOI: 10.1039/C8NR02052C

crystallinity than MFC/graphene composites. This is due to hydrogen bonding between RGO and MFC molecules that significantly restricts the molecular movement of cellulose.

Table 3 Crystallinity of neat MFC together with MFC/graphene and MFC/RGO at different loadings. The crystallinity is estimated by Segal's method [49].

Filler loading	MFC/graphene	MFC/RGO
MFC 100 %	61.50	
1 wt%	65.30	63.28
5 wt%	67.11	64.59
9 wt%	64.27	62.02

To achieve the best properties of the reinforced composites, the filler must be homogeneously dispersed in the polymer matrix to allow for an efficient load transfer between the filler and the matrix [50]. The surface chemistry of pristine graphene makes it unsuitable as a reinforcement in most hydrophilic polymer matrices, because graphene tends to agglomerate [51] and, thus, has poor interaction with the aqueous matrix. Functionalised graphene, such as GO and RGO offers the best compatibility potential due to the presence of oxygen functional groups on the surface and edges. The mass distribution of RGO and graphene in the MFC matrix was studied by AMBERTEC Beta Formation Tester. In Figure 6, the specific formation number of the neat MFC films is shown in comparison with different graphene and RGO loadings. High specific number means poor distribution of the mass (inhomogeneity) in the film. From the results, it is clearly visible that the high shear exfoliation of graphene in the presence of the MFC suspension significantly helps to distribute the material homogeneously and stabilise the filler in the MFC matrix. The results are closely comparable to that of functionalised RGO, which, in theory, is better equipped to disperse in aqueous medium than pristine graphene due to the presence of functional groups. This shows that the novel approach of high shear

View Article Online
DOI: 10.1039/C8NR02052C

exfoliation in the presence of MFC, and the amphiphilic nature of MFC, successfully promotes homogenous dispersion of graphene in the matrix. Graphene and RGO help also to disperse the MFC and prevent flocculation. Thus, they act like a particulate dispersant helping to distribute the mass evenly and make an even formation. The improvement in formation is very large compared to the neat MFC, especially for the RGO reinforced composites. These results are in supportive agreement with the XRD crystallinity assessment in the previous section.

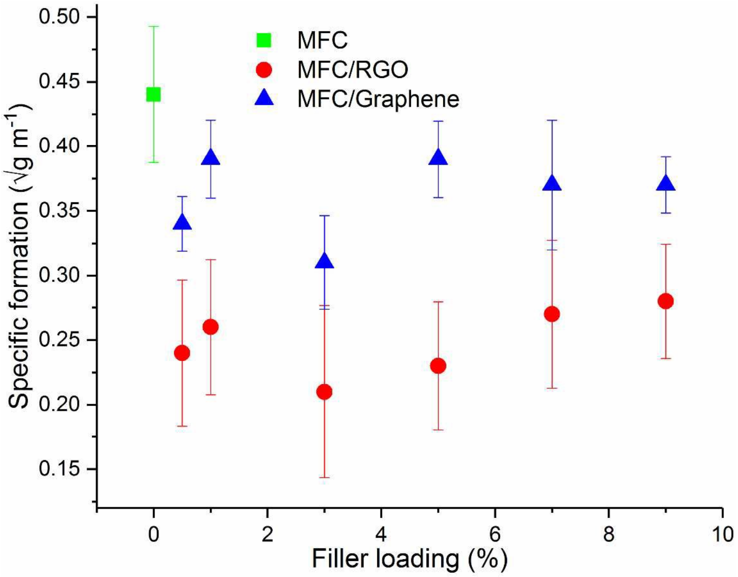

Figure 6 Specific formation number of MFC, MFC/Graphene and MFC/RGO composite films as a function of filler loading.

View Article Online
DOI: 10.1039/C8NR02052C

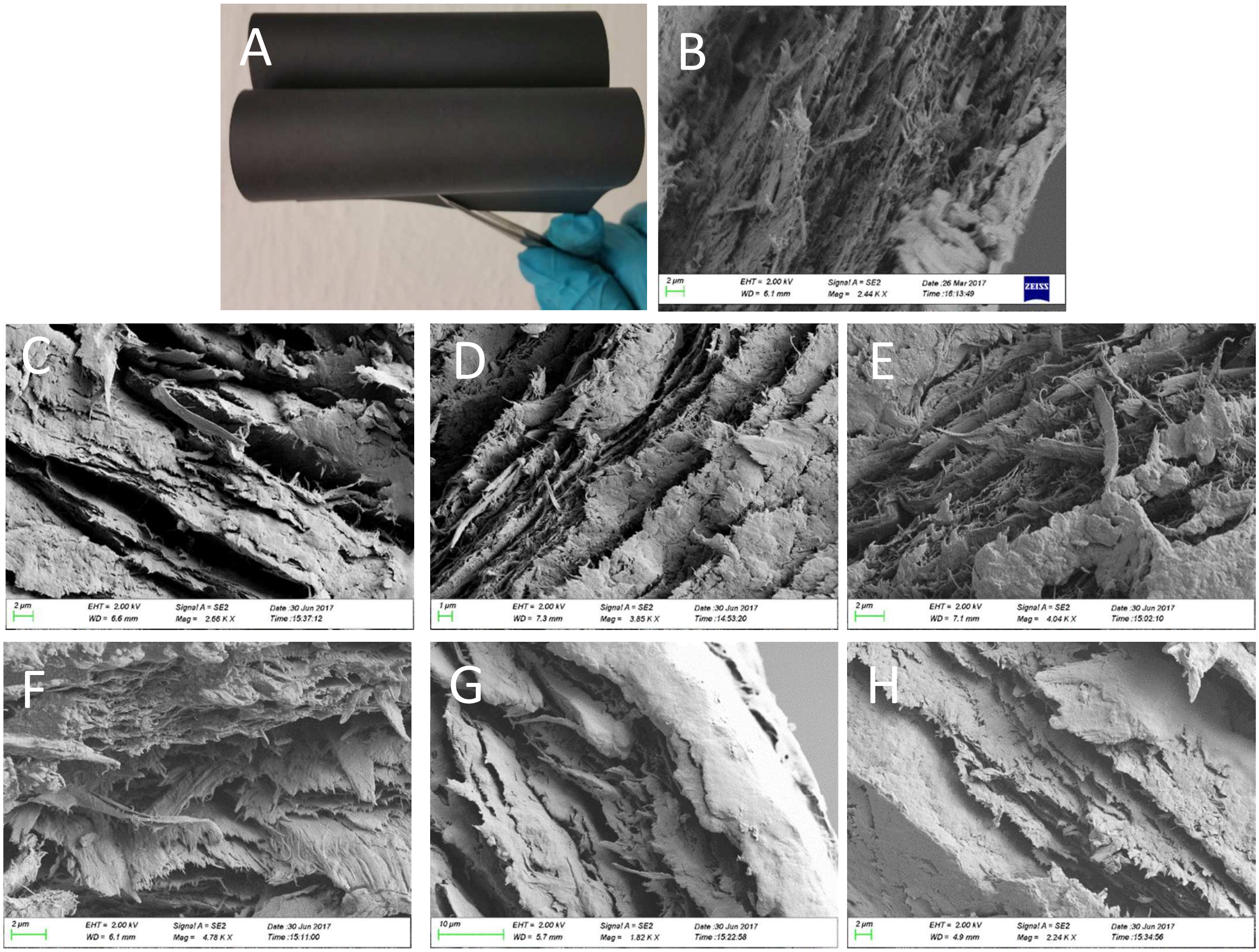

Figure 7 (A) Picture of the flexible films and SEM images of cross-section area of (B) neat MFC, (C) - (E) graphene/MFC, and (F) - (H) RGO/MFC composites with various filler loadings of 1, 5 and 9 wt%, respectively

Figure 7 shows the cross-section of the neat MFC with different loading of RGO and graphene content. The neat MFC shows a highly fibrous network structure consisting of randomly ordered cellulose fibrils. Both graphene and RGO reinforced composites show a similar dense and compact layered homogeneous structure, although for the graphene/MFC composites more cellulose fibrils are visible confirming poorer interaction than that of RGO reinforced composites. The images also show layered type morphology with the sheets arranged parallel to the surface of the films.

The mechanical properties of the graphene/MFC composites depend on the interaction between graphene and the MFC matrix as well as graphene dispersion in the MFC matrix. Figure 8 shows the

View Article Online
DOI: 10.1039/C8NR02052C

typical stress-strain curves for the neat MFC together with various loadings of graphene and RGO. The neat MFC, graphene/MFC and RGO/MFC composites show a typical brittle character with no specific yield point observed. Similar results were also observed in another study for GO and bacterial cellulose [45]. Compared with the neat MFC, the tensile strength increased and then decreased with further loading of graphene, whilst for the RGO/MFC composites a higher tensile strength is seen at all filler loading content, as shown in Figure 9A. Figure 9B also shows that the Young's modulus was enhanced with the incorporation of co-exfoliated graphene and RGO. For example, at 1 wt% loading, the tensile strength for the graphene/MFC and RGO/MFC composites increased by 24 % and 48 %, whilst the Young's modulus increased by 16 % and 27 %, respectively. The greater enhancement observed for the RGO reinforced MFC composites is due to the oxygen containing groups that promote a strong interaction or hydrogen bonding between RGO and the MFC matrix, and thus provide an intimately bonded medium for stress transfer. The functional groups also promote a homogeneous dispersion of RGO in the MFC matrix, which is also vital for high performance composites [19]. Due to the hydrophobic nature of pristine graphene, it has a strong tendency to aggregate in hydrophilic medium. The increase in graphene loading led to the deterioration of tensile strength due to the increase of the aggregates in the MFC matrix, which disrupts the MFC fibre network and creates voids, due to a weak interaction with the MFC matrix, and, thus, high local stresses.

The enhancement of the mechanical properties at lower loading of pristine graphene cellulose materials was also observed in other studies [52-54]. This enhancement suggests that there is some form of interaction that takes place between graphene and the MFC matrix. It has been shown that MFC exhibits amphiphilic properties [55], which might explain the enhancement of the properties due to the interaction of graphene and the hydrophobic part of MFC. It has also been suggested that the bonding between graphene and MFC matrix could be due to the π-interactions [52, 56]. Similar interactions that are observed between proteins and carbohydrates, for example, enzymes bonding to the (110) crystalline

View Article Online
DOI: 10.1039/C8NR02052C

cellulose surface [57] as well as binding of cellulose chains in hydrolytic enzymes [58]. This strong adhesion between graphene and MFC ensures that there is an efficient stress transfer from graphene to the MFC matrix. Moreover, the high shear co-exfoliation process provides an extreme blending/dispersing environment of graphene and the MFC. As graphene is exfoliated, the cellulosic species are exposed to the fresh graphene surface and, in most cases, the surface energy of a fresh surface is higher than on an aged surface, which in turn has adsorbed other stabilising species prior to the exposure to cellulose. This effect has been seen for co-grinding and co-homogenising of MNFC with pigments [59], where the mechanical properties of the composite were enhanced.

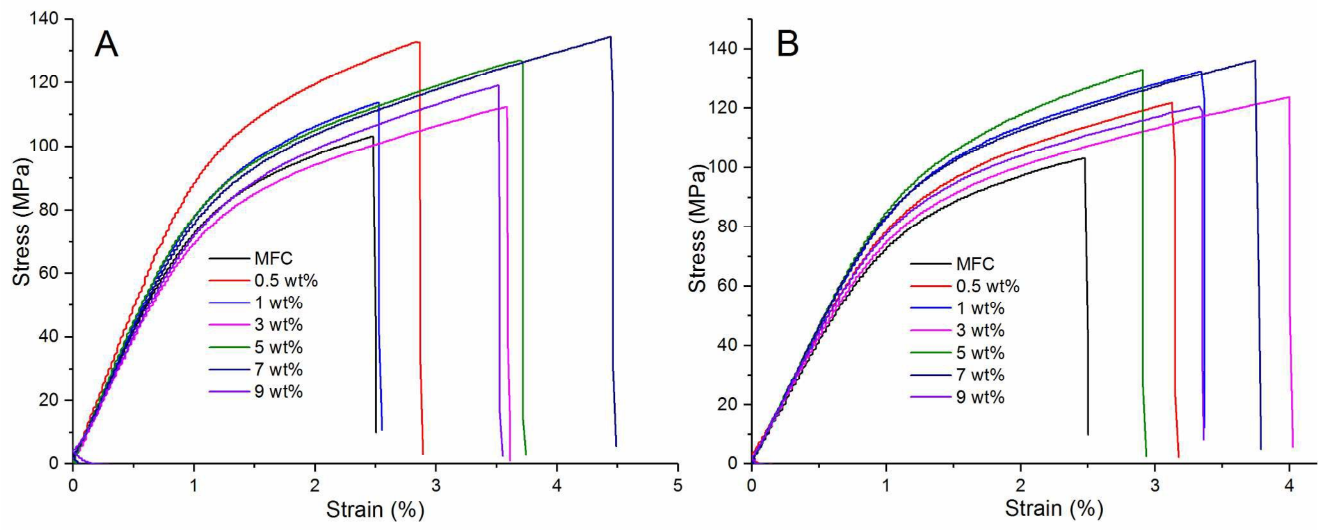

Figure 8 Stress-strain curves of the neat MFC and with different loadings of graphene and RGO: (A) MFC/graphene, and (B) MFC/RGO composites

The decrease in the mechanical properties at higher graphene content can be explained as being due to the aggregation of graphene in the polymer matrix. Even though MFC can be considered as amphiphilic, in practice it is displaying a surface orientation which is highly hydrophilic in aqueous medium, with only a small hydrophobic part, which is probably hidden in a micelle-like structure. Therefore, as the graphene concentration is increased, the hydrophobic-hydrophobic interaction between graphene sheets becomes greater than the hydrophobic-hydrophobic interaction between graphene and MFC. This leads to a weaker interaction between graphene and the MFC matrix,

View Article Online
DOI: 10.1039/C8NR02052C

resulting in debonding of graphene from MFC fibres as well as a disruption of the MFC network ordering by large graphene aggregates.

Despite the brittle nature of the composites, the breaking strain for the graphene/MFC and RGO/MFC composites both showed a slight increase when compared to the neat MFC, Figure 9C. This can be related to the noncovalent bonding between the filler and MFC fibrils, which can lead to sliding of the graphene sheets.

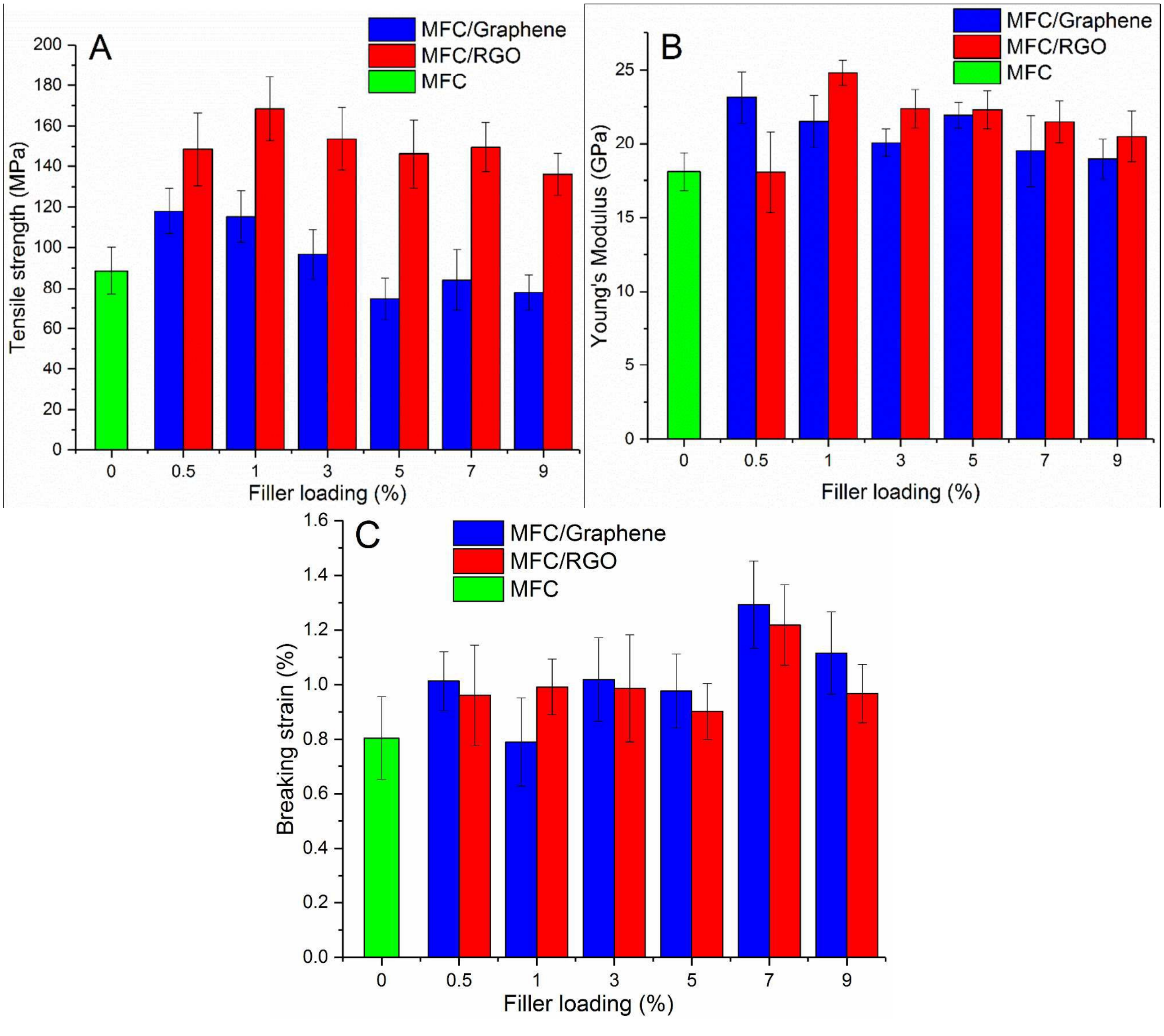

Figure 9 Mechanical properties of the composites as a function of filler loading of graphene or RGO: (A) tensile strength, (B) Young's modulus, (C) tensile index, and (D) break elongation. (A colour version of this Figure can be viewed online.)

View Article Online
DOI: 10.1039/C8NR02052C

The optical properties of the MFC can be changed by incorporation of graphene and RGO. Figure 10 shows the light scattering of the composites with different filler loading. A significant decrease is observed for both MFC/RGO and MFC/graphene composites as compared to the neat MFC. However, as expected, the light scattering for the RGO/MFC composites is much less than that for the graphene/MFC composites. These results are in close agreement with the nitrogen adsorption/desorption measurements. Functionalised RGO forms a dense and more intact structure due to the strong interaction with the MFC fibrils, thus lower light scattering power is exhibited by these films in comparison to graphene reinforced MFC composites.

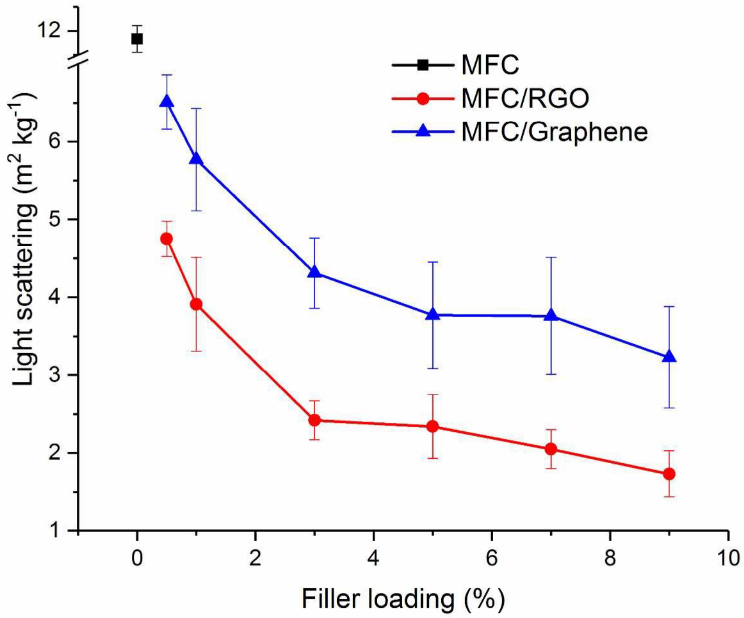

Figure 10 The light scattering of the neat MFC films, MFC/RO and MFC/graphene composites

TGA was employed to study the thermal stability of the produced composites, with results as shown in Figure 11 together with the differential thermogravimetry data. The thermal stability of the composites was enhanced by incorporation of both RGO and graphene compared to the neat MFC. Compared to the neat MFC, however, both RGO and graphene reinforced MFC composited materials showed enhanced thermal stability. For example, at 400 ^{o}C at 9 wt% filler loading, the resistance to

View Article Online
DOI: 10.1039/C8NR02052C

thermal degradation of the RGO/MFC and graphene/MFC composites increased by 36 % and 22 %, respectively. Interestingly, RGO reinforced composites showed better thermal stability than graphene. This is probably due to the consolidation effect between the filler and the MFC matrix [60]. RGO contains oxygen functional groups that promote a strong interaction and bonding with the MFC fibrils. The RGO sheets completely cover the fibrils and thus prevent exposure of the fibrils to heat. However, due to lack of strong molecular interaction between graphene and MFC fibrils, the fibrils are more exposed externally and thus undergo thermal degradation more readily, and, hence, the graphene/MFC composites showed a comparatively lower thermal stability.

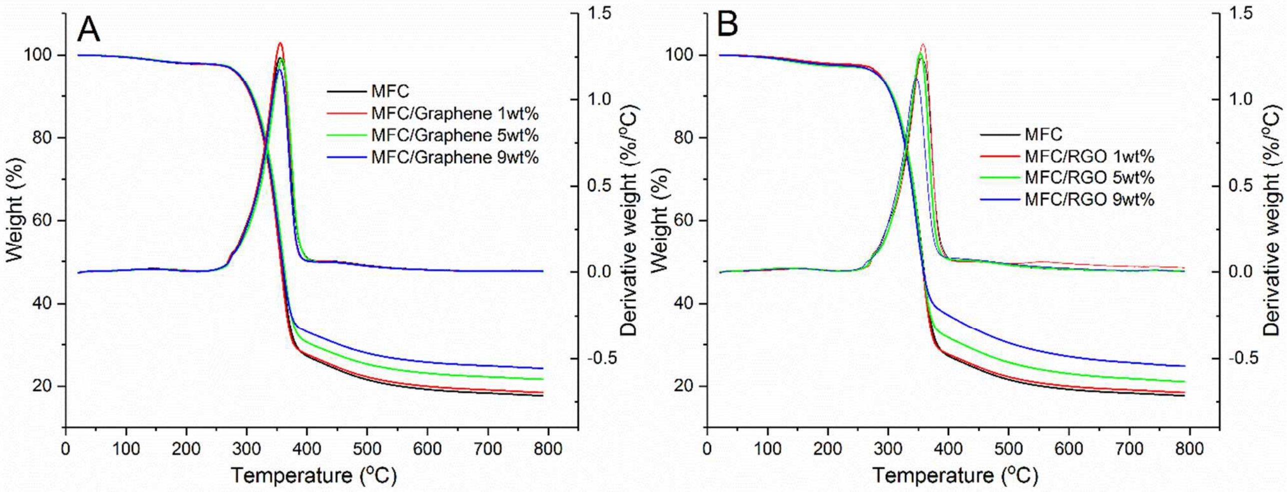

Figure 11 Comparison of TGA and DTG curves of neat MFC nanocomposites with the addition of 1, 5, 9 wt% of graphene (A), and RGO (B)

The amount of residual char (residuum) is also a good indicator of the thermal stability of the material. At 800 °C for the 9 wt% filler loaded composites, the residual char increased by 40 % and 37 % for the RGO/MFC and graphene/MFC composites, respectively. Due to the strong interaction of RGO and the MFC matrix, the mobility of MFC fibrils at the interface between RGO and MFC is significantly suppressed as compared to that of graphene and MFC, and, thus, a higher amount of char or carbon of MFC deposits at the interface [61]. Another reason for the enhancement of the thermal

View Article Online
DOI: 10.1039/C8NR02052C

stability of the composites is attributed to the platelet structure of the filler. The graphene and RGO sheets promote a layered type of structure within the composite, as shown in the SEM images in Figure 7, which provides an undisturbed lateral route for the volatile degradation products to escape and at the same time reduces significantly the decomposition rate of the whole composite [44].

The specific surface area of the composites and pore size distribution within them were analysed using the Barrett-Joyner-Halenda (BJH) method. In several applications, the effective surface area and pore structure of the composite in an aqueous medium are important. One way to study the pore structure in this case is to use a critical point drying (CPD) method to prepare an aerogel from the composite. In CPD, the water is exchanged for acetone, and then to liquid CO_2 which is evaporated above the critical point. Since surface tension under these conditions is negligible, consolidation effects are largely avoided. The pore structure measured with nitrogen sorption is representative of the pore structure in the wet state.

Figure 12 shows the nitrogen adsorption/desorption isotherms with inserts displaying the pore size distribution, analysed by the BJH method, of individual MFC, RGO and graphite as well as MFC/graphene and MFC/RGO composites at 0.5 and 9 wt% filler loading. It is interesting to note that, with the addition of only 0.5 wt% of graphene, the specific surface area (SSA) increases from 217 to 272 $m^2 g^{-1}$ and maintains much of the pore volume, as shown in Table 4. RGO, however, does not show this effect. At 9 wt% filler loading, both the graphene and RGO composites showed a slight increase of SSA whilst the pore volume remained the same. It is possible that the strong hydrophobic interactions of the graphene are helping to space the MFC and create a higher effective surface area. RGO, on the other hand, hydrogen bonds to the MFC and packs in more densely, spaced within the MFC network, leading to a lower surface area and less pore volume. Impact on potential adsorption differences due to the more open structure generated when using pure graphene remain at this stage a point of conjecture.

View Article Online
DOI: 10.1039/C8NR02052C

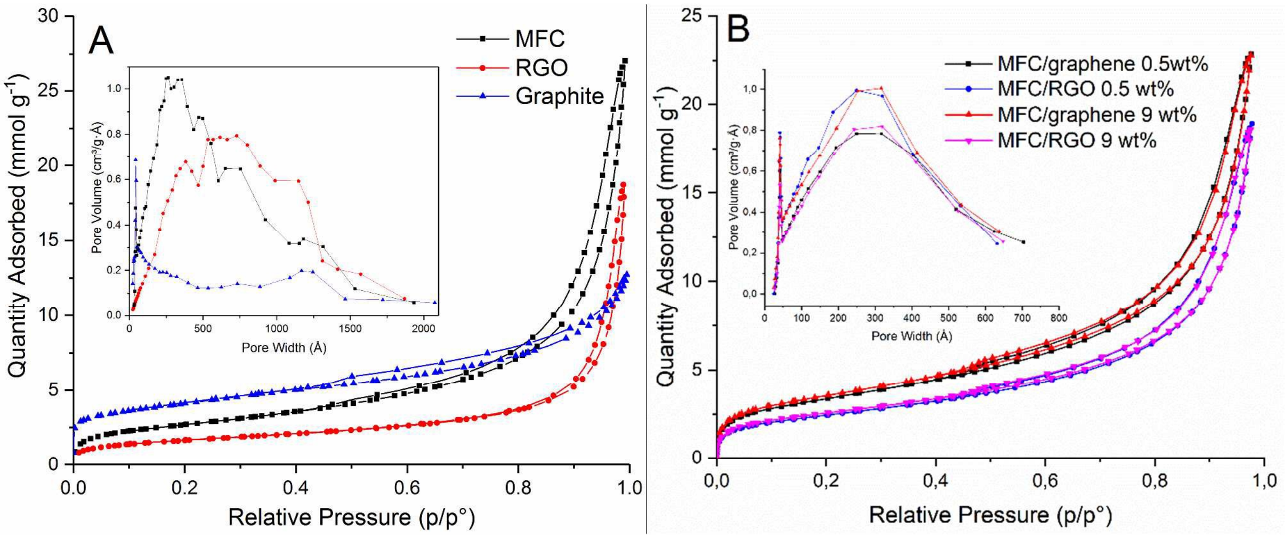

Figure 12 Nitrogen adsorption/desorption isotherms of (A) MFC, RGO and graphite, and (B) MFC/graphene MFC/RGO composites with 0.5 and 9 wt% filler loading; the inserts show the pore size distribution

Table 4 Nitrogen sorption results showing the specific surface area (SSA) and pore volume

Samples	SSA, $m^2\ g^{-1}$	Pore volume, $cm^3\ g^{-1}$
MFC	217.83	0.90
RGO	131.20	0.59
Graphite	316.14	0.40
MFC/graphene 0.5 wt%	272.82	0.82
MFC/graphene 9 wt%	286.52	0.81
MFC/RGO 0.5 wt%	197.67	0.68
MFC/RGO 9 wt%	206.00	0.66

The wide range of pore size distribution might suggest that the composites have potential for application in capacitive desalination technologies, for example [62]. Combination of the meso- and macropores improves the overall efficiency of the composite by enabling a high mass transfer to the mesopores as well as facilitating the formation of an electrical double-layer in the mesopores. Another advantage of these composites for this application is that MFC provides the property of hydrophilicity

View Article Online
DOI: 10.1039/C8NR02052C

that is essential for the formation of an electrical double-layer by enhancing adsorption and storage of ions in the inner structure of the composite in aqueous medium [63]. These properties also provide the potential possibility for application in energy storage devices as electrodes. The hydrophilic MFC can be effectively used as electrolyte nano-reservoirs, which can reduce ion transport distance in the mesopores [64]. Moreover, highly hydrophilic MFC exhibits excellent re-swelling properties in aqueous based electrolyte.

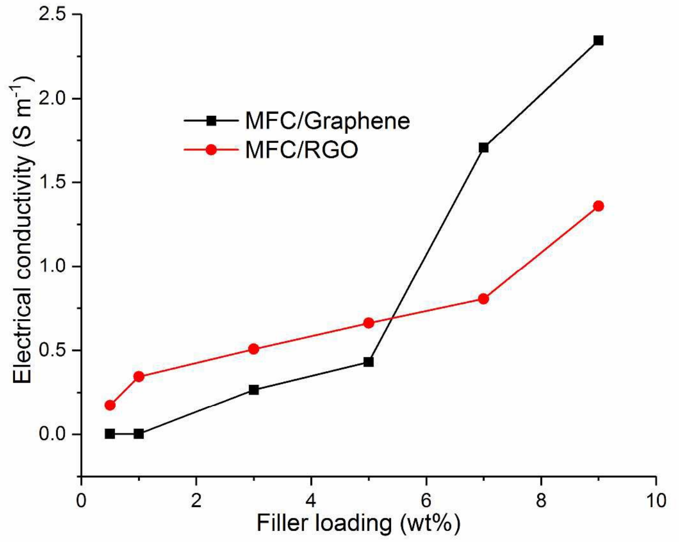

Figure 13 Electrical conductivity of MFC/graphene and MFC/RGO composite films with various concentrations of filler loading.

The electrical properties of the composite films were measured by a four-probe technique and the results are shown in Figure 13. The neat MFC films are nonconductive. At lower concentration of 0.5 wt% filler loading, the RGO/MFC films already showed conductivity, whilst the graphene/MFC films were still insulators. This is due to the homogeneous dispersion of RGO in the MFC matrix, which enables a complete network of conductive RGO sheets to be formed. However, poor graphene dispersion means that there are still gaps causing discontinuity of the matrix, thus there is an incomplete network of conductive graphene sheets. At higher concentration, however, for example at 9 wt% loading, a high electrical conductivity of about 2.4 S m^{-1} is observed for the graphene/MFC

View Article Online
DOI: 10.1039/C8NR02052C

composites whilst limited to 1.4 S m^{-1} for the RGO/MFC composites. The difference is due to the presence of defects in RGO caused by the prior oxidation step.

4. Conclusions

Graphene exhibits exceptional functional properties that can be applied in various applications. The amphiphilic properties of MFC originating from the O-H and C-H groups support the concept to use it as an ideal material for fabrication of graphene-based composites. In this study, we have shown that few layer graphene can be successfully formed by co-exfoliation of graphite in aqueous MFC suspension by application of high shear. Composites can be derived from the mix of MFC and graphene produced in this manner, which are superior to simple mixing of MFC with separately exfoliated graphene. Such composites are, therefore, principally based on renewable materials and are fabricated using a simple and environmentally friendly method, being highly desirable especially for large scale application. Formation analysis tests showed that graphene was homogeneously dispersed in the MFC matrix, which is vital for producing high performance composites. The composites showed enhanced mechanical, electrical, thermal stability and optical properties. Due to these various excellent functional properties, the composites produced in this novel way have potential application in conductive flexible films, energy storage devices, biosensors, UV-protection, absorbents, ion filters etc.

ACKNOWLEDGEMENT

The authors appreciate financial support from Omya International AG. This work made use of the Aalto University Nanomicroscopy Centre (Aalto-NMC) for SEM imaging and XRD analysis, and Aalto University Bioeconomy Facilities (XPS). The authors would also like to extend their appreciation to Asbury Carbons for the supply of free graphite samples.

COMPLIANCE WITH ETHICAL STANDARDS

DOI: 10.1039/C8NR02052C

CONFLICT OF INTEREST

The authors declare that they have no conflict of interest.

References

1. K. S. Novoselov, A. K. Geim, S. V. Morozov, D. Jiang, Y. Zhang, S. V. Dubonos, I. V. Grigorieva and A. A. Firsov, *Science,* 2004, **306**, 666-669.

2. K. S. Novoselov, V. I. Fal'ko, L. Colombo, P. R. Gellert, M. G. Schwab and K. Kim, *Nature,* 2012, **490**, 192-200.

3. F. Zhang, T. Zhang, X. Yang, L. Zhang, K. Leng, Y. Huang and Y. Chen, *Energy Environ Sci,* 2013, **6**, 1623.

4. H. Wang, Q. Hao, X. Yang, L. Lu and X. Wang, *Nanoscale,* 2010, **2**, 2164-2170.

5. H. Cong, J. Chen and S. Yu, *Chem. Soc. Rev.,* 2014, **43**, 7295-7325.

6. H. Cong, X. Ren, P. Wang and S. Yu, *ACS Nano,* 2012, **6**, 2693-2703.

7. H. Tai, Y. Zhen, C. Liu, Z. Ye, G. Xie, X. Du and Y. Jiang, *Sensors Actuators B: Chem.,* 2016, **230**, 501-509.

8. J. Phiri, P. Gane and T. C. Maloney, *Mater. Sci. Eng. , B,* 2017, **215**, 9-28.

9. R. Raccichini, A. Varzi, S. Passerini and B. Scrosati, *Nat. Mater.,* 2015, **14**, 271-279.

10. T. Ramanathan, A. A. Abdala, S. Stankovich, D. A. Dikin, M. Herrera-Alonso, R. D. Piner, D. H. Adamson, H. C. Schniepp, X. Chen, R. S. Ruoff, S. T. Nguyen, I. A. Aksay, R. K. Prud'Homme and L. C. Brinson, *Nat. Nanotechnol.,* 2008, **3**, 327-331.

11. I. Zaman, H. Kuan, Q. Meng, A. Michelmore, N. Kawashima, T. Pitt, L. Zhang, S. Gouda, L. Luong and J. Ma, *Adv. Funct. Mater.,* 2012, **22**, 2735-2743.

12. A. S. Patole, S. P. Patole, H. Kang, J. Yoo, T. Kim and J. Ahn, *J. Colloid Interface Sci.,* 2010, **350**, 530-537.

13. T. Kuilla, S. Bhadra, D. Yao, N. H. Kim, S. Bose and J. H. Lee, *Prog. Polym. Sci.,* 2010, **35**, 1350-1375.

14. S. Park, D. A. Dikin, S. T. Nguyen and R. S. Ruoff, *J. Phys. Chem. C,* 2009, **113**, 15801-15804.

15. V. Dhand, K. Y. Rhee, H. Ju Kim and D. Ho Jung, *J Nanomater.,* 2013, **2013**, 14.

16. G. Pandey and E. T. Thostenson, *Polym. rev.,* 2012, **52**, 355-416.

View Article Online
DOI: 10.1039/C8NR02052C

17. R. J. Moon, A. Martini, J. Nairn, J. Simonsen and J. Youngblood, *Chem. Soc. Rev.,* 2011, **40**, 3941-3994.

18. D. Klemm, F. Kramer, S. Moritz, T. Lindstrom, M. Ankerfors, D. Gray and A. Dorris, *Angew. Chem. Int. Ed Engl.,* 2011, **50**, 5438-5466.

19. K. Hu, D. D. Kulkarni, I. Choi and V. V. Tsukruk, *Prog. Polym. Sci.,* 2014, **39**, 1934-1972.

20. W. S. Hummers and R. E. Offeman, *J. Am. Chem. Soc.,* 1958, **80**, 1339.

21. B. C. Brodie, *Philosophical Transactions of the Royal Society of London,* 1859, **149**, 249-259.

22. M. Segal, *Nat Nano,* 2009, **4**, 612-614.

23. M. Yi and Z. Shen, *J. Mater. Chem. A,* 2015, **3**, 11700-11715.

24. M. Moniruzzaman and K. I. Winey, *Macromolecules,* 2006, **39**, 5194-5205.

25. J. Phiri, P. Gane and T. C. Maloney, *J. Mater. Sci.,* 2017, **52**, 8321-8337.

26. K. R. Paton, E. Varrla, C. Backes, R. J. Smith, U. Khan, A. O'Neill, C. Boland, M. Lotya, O. M. Istrate, P. King, T. Higgins, S. Barwich, P. May, P. Puczkarski, I. Ahmed, M. Moebius, H. Pettersson, E. Long, J. Coelho, S. E. O'Brien, E. K. McGuire, B. M. Sanchez, G. S. Duesberg, N. McEvoy, T. J. Pennycook, C. Downing, A. Crossley, V. Nicolosi and J. N. Coleman, *Nat. Mater.,* 2014, **13**, 624-630.

27. Y. Wei and Z. Sun, *Curr. Opin. Colloid Interface Sci,* 2015, **20**, 311-321.

28. H. Kangas, P. Lahtinen, A. Sneck, A. Saariaho, O. Laitinen and E. Hellen, *NORD PULP PAP RES J,* 2014, **29**, 129-143.

29. T. C. Maloney, *Holzforschung,* 2015, **69**, 207.

30. J. Rantanen, K. Dimic-Misic, J. Kuusisto and T. C. Maloney, *Cellulose,* 2015, **22**, 4003-4015.

31. L. Johansson and J. M. Campbell, *Surf. Interface Anal.,* 2004, **36**, 1018-1022.

32. D. Li, M. B. Muller, S. Gilje, R. B. Kaner and G. G. Wallace, *Nat. Nanotechnol,* 2008, **3**, 101-105.

33. C. Casiraghi, S. Pisana, K. S. Novoselov, A. K. Geim and A. C. Ferrari, *Appl. Phys. Lett.,* 2007, **91**, 233108.

34. A. C. Ferrari, *Solid State Commun.,* 2007, DOI: http://dx.doi.org/10.1016/j.ssc.2007.03.052.

35. S. Eigler, C. Dotzer and A. Hirsch, *Carbon,* 2012, DOI: http://dx.doi.org/10.1016/j.carbon.2012.03.039.

36. L. G. Cancado, A. Jorio, E. H. Martins Ferreira, F. Stavale, C. A. Achete, R. B. Capaz, M. V. O. Moutinho, A. Lombardo, T. S. Kulmala and A. C. Ferrari, *Nano Lett.,* 2011, **11**, 3190-3196.

37. A. C. Ferrari, J. C. Meyer, V. Scardaci, C. Casiraghi, M. Lazzeri, F. Mauri, S. Piscanec, D. Jiang, K. S. Novoselov, S. Roth and A. K. Geim, *Phys. Rev. Lett.,* 2006, **97**, 187401.

38. S. Das, F. Irin, H. S. Tanvir Ahmed, A. B. Cortinas, A. S. Wajid, D. Parviz, A. F. Jankowski, M. Kato and M. J. Green, *Polymer,* 2012, **53**, 2485-2494.

39. D. Parviz, S. Das, H. S. T. Ahmed, F. Irin, S. Bhattacharia and M. J. Green, *ACS Nano,* 2012, **6**, 8857-8867.

40. S. Park, K. S. Lee, G. Bozoklu, W. Cai, S. T. Nguyen and R. S. Ruoff, *ACS Nano,* 2008, **2**, 572-578.

41. Y. Zhang, H. Li, X. Li, M. E. Gibril, K. Han and M. Yu, *J. Poly. Res.,* 2013, **20**, 171.

42. M. Schwanninger, J. C. Rodrigues, H. Pereira and B. Hinterstoisser, *Vib. Spectrosc.,* 2004, DOI: http://dx.doi.org/10.1016/j.vibspec.2004.02.003.

43. T. Kondo, *J. Polym. Sci. Part B Polym. Phys.,* 1994, **32**, 1229-1236.

44. L. Yao, Y. Lu, Y. Wang and L. Hu, *Carbon,* 2014, DOI: http://dx.doi.org/10.1016/j.carbon.2013.12.066.

45. Y. Feng, X. Zhang, Y. Shen, K. Yoshino and W. Feng, *Carbohydr. Polym.,* 2012, **87**, 644-649.

46. R. Wu, X. Wang, Y. Wang, X. Bian and F. Li, *Ind Eng Chem Res,* 2009, **48**, 7132-7136.

47. N. Kumar, C. Huang, P. Yen, W. Wu, K. Wei and T. Y. Tseng, *RSC Adv.,* 2016, **6**, 60578-60586.

48. W. Ouyang, J. Sun, J. Memon, C. Wang, J. Geng and Y. Huang, *Carbon,* 2013, **62**, 501-509.

49. L. Segal, J. J. Creely, A. E. Martin and C. M. Conrad, *Text. Res. J.,* 1959, **29**, 786-794.

50. A. S. Wajid, S. Das, F. Irin, H. S. T. Ahmed, J. L. Shelburne, D. Parviz, R. J. Fullerton, A. F. Jankowski, R. C. Hedden and M. J. Green, *Carbon,* 2012, **50**, 526-534.

51. J. Wei, T. Vo and F. Inam, *RSC Adv.,* 2015, **5**, 73510-73524.

52. J. M. Malho, P. Laaksonen, A. Walther, O. Ikkala and M. B. Linder, *Biomacromolecules,* 2012, **13**, 1093-1099.

53. B. Wang, W. Lou, X. Wang and J. Hao, *J. Mater. Chem.,* 2012, **22**, 12859-12866.

54. H. Zhang, Z. Wang, Z. Zhang, J. Wu, J. Zhang and J. He, *Adv Mater,* 2007, **19**, 698-704.

55. L. Johansson, T. Tammelin, J. M. Campbell, H. Setala and M. Osterberg, *Soft Matter,* 2011, **7**, 10917-10924.

56. F. A. Quiocho, *Biochem. Soc. Trans.,* 1993, **21**, 442.

View Article Online
DOI: 10.1039/C8NR02052C

57. J. Lehtio, J. Sugiyama, M. Gustavsson, L. Fransson, M. Linder and T. T. Teeri, *Proc. Natl. Acad. Sci.,* 2003, **100**, 484-489.

58. C. Divne, J. Ståhlberg, T. T. Teeri and T. A. Jones, *J. Mol. Biol,* 1998, DOI: http://dx.doi.org/10.1006/jmbi.1997.1437.

59. M. Schenker, J. Schoelkopf, P. Mangin and P. Gane, *Tappi J.,* 2016, **15**, 405-416.

60. J. Rantanen and T. C. Maloney, *Eur. Polym. J.,* 2015, DOI: http://dx.doi.org/10.1016/j.eurpolymj.2015.03.045.

61. C. Kim, W. Khan, D. Kim, K. Cho and S. Park, *Carbohydr. Polym.,* 2011, **86**, 903-909.

62. P. Wang, G. Lu, H. Yan, W. Ni, M. Xu, Y. Xue and Y. Yan, *RSC Adv.,* 2016, **6**, 70532-70536.

63. Z. Sui, Q. Meng, J. Li, J. Zhu, Y. Cui and B. Han, *J. Mater. Chem. A,* 2014, **2**, 9891-9898.

64. K. Gao, Z. Shao, J. Li, X. Wang, X. Peng, W. Wang and F. Wang, *J. Mater. Chem. A,* 2013, **1**, 63-67.